Chemical Science

Accepted Manuscript

This article can be cited before page numbers have been issued, to do this please use: T. Huo, Q. Yang, G. Yu, M. Li, X. Bai, T. Lv, X. Zhang, J. Xu, K. Liu, X. Zhou, X. Tan, L. Li, K. Lei and S. Zheng, *Chem. Sci.*, 2026, DOI: 10.1039/D6SC01783E.




ROYAL SOCIETY OF CHEMISTRY

rsc.li/chemical-science

View Article Online
DOI: 10.1039/D6SC01783E

ARTICLE

# Regulation of Local Chemistry in O3-type Layered Oxide Cathodes for Practical Sodium-Ion Batteries

Received 00th January 20xx,
Accepted 00th January 20xx

DOI: 10.1039/x0xx00000x

Tongtong Huo,[a] Qian Yang,[a] Genliang Yu,[a] Mingyue Li,[a] Xuejie Bai,[a] Ting Lv,[a] Xiaobo Zhang,[a] Jie Xu,[a] Kai Liu,[a] Xunzhu Zhou,[b] Xin Tan, [b,c] Lin Li,*[b,c] Kaixiang Lei,*[a] and Shijian Zheng,*[a]

O3-type layered oxide cathodes have emerged as promising candidates for advanced sodium-ion batteries (SIBs) due to their high theoretical specific capacity. However, undesirable phase transitions, irreversible $O_2$ release, and transition metal (TM) ions dissolution severely deteriorate their long-cycle stability. Herein, a cation-anion dual-site high-entropy doping strategy is proposed to modulate the local chemistry of O3-type layered oxide cathodes, aiming to enhance the covalency of TM-O bonds. The robust covalent TM-O bonds can effectively suppress adverse phase transitions, inhibit irreversible oxygen redox reactions, and reduce $TM^{n+}$ dissolution. Consequently, $NaNi_{0.25}Fe_{0.14}Mn_{0.3}Li_{0.1}Ti_{0.15}Cu_{0.03}Zn_{0.03}O_{1.94}F_{0.06}$ (HEO) delivers a high specific capacity of 152.27 mAh $g^{-1}$ and a capacity retention of 73.69% after 500 cycles. More importantly, HEO exhibits impressive temperature tolerance, superior air stability and acceptable full-cell performance, demonstrating its huge potential for practical SIBs application. This work develops a versatile cation-anion dual-site high-entropy doping strategy to modulate the local chemistry of O3-type layered oxide cathodes, furnishing a robust foundation for advancing cathode materials for practical SIBs.

## Introduction Experimental

Sodium-ion batteries (SIBs) hold great promise as a pivotal technology for large-scale energy storage systems due to their abundant resource reserves and low production costs.[1-3] As a core component of SIBs, cathode materials have a critical impact on their electrochemical performance, technological development potential, and practical application prospects.[4] Among the discovered cathode materials, O3-type layered oxide cathodes ($Na_xTMO_2$, where x > 0.7, TM represents transition metal) demonstrate broad application prospects due to their high theoretical specific capacity.[5-6] However, during the charge/discharge process of the O3-NFM (O3-$NaNi_{0.4}Fe_{0.2}Mn_{0.4}O_2$) cathode, the deintercalation of $Na^+$ and the oxidation of $TM^{n+}$ induce continuous variations in the unit cell parameters. Particularly under high-voltage conditions exceeding 4.0 V, this triggers an unfavorable P3→O3' phase transition, thereby resulting in severe volume changes.[7-8] Furthermore, the excessive oxidative participation of lattice oxygen exposes the inherently weak TM-O bonds to a higher risk of disruption: It not only readily forms O-O dimers, ultimately resulting in the irreversible release of lattice oxygen in the form of $O_2$, but the cleavage of TM-O bonds also creates conditions for the additional irreversible dissolution of $TM^{n+}$.[9-11] This leads to a reduction in the number of active TM sites, exacerbates interfacial side reactions, and triggers the initiation of intragranular cracks.[12-13] Collectively, these complex detrimental effects ultimately induce an irreversible phase transition of the cathode material from a layered structure to a rock-salt phase, resulting in permanent structural damage with fast capacity degradation.[14-15]

In general, the TM-O bonds serve as the core structural framework of layered oxide cathode materials, and the insufficiency of its covalency is the intrinsic cause triggering the aforementioned performance degradation issues.[16-18] Therefore, regulating the covalency of TM-O bonds is regarded as an effective strategy to boost the sodium storage performance of O3-type layered oxide cathodes.[19-22] To date, element doping, as a facile and efficient modification strategy, has been extensively adopted to optimize the local chemistry of O3-type layered oxide cathode materials.[23-25] Nevertheless, conventional single/double-element doping strategies exhibit certain limitations, failing to simultaneously address multiple issues including phase structure distortion, lattice oxygen release, and transition metal ions dissolution.[7,26] In recent years, the high-entropy doping strategy, relying on the synergistic effect of multiple elements, has demonstrated unique advantages in precisely regulating the local chemistry of layered oxide cathode materials and stabilizing the lattice framework, thereby providing a novel paradigm for the performance breakthrough of electrode materials.[27-28] However, most existing studies on high-entropy doping are confined to the modification of cation sites, failing to give full play to the synergistic regulation effect of both anions and cations.[29-32] Its modulation effect on the covalency of TM-O bonds is limited, making

[a] Tianjin Key Laboratory of Materials Laminating Fabrication and Interface Control Technology, School of Materials Science and Engineering, Hebei University of Technology, Tianjin 300401, China E-mail: kaixianglei@hebut.edu.cn; sjzheng@hebut.edu.cn
[b] Institute for Carbon Neutralization Technology, College of Chemistry and Materials Engineering, Wenzhou University, Wenzhou, Zhejiang 325035, China E-mail: linli@wzu.edu.cn
[c] Zhejiang Provincial Key Laboratory of Advanced Battery Materials and Technology, Wenzhou University Technology Innovation Institute for Carbon Neutralization, Zhejiang 325035, China
Electronic Supplementary Information (ESI) available: [details of any supplementary information available should be included here]. See DOI: 10.1039/x0xx00000x

View Article Online
DOI: 10.1039/D5SC01787F





it difficult to fundamentally overcome the performance degradation bottleneck of O3-type layered oxide cathodes.[33-34]

Herein, we propose a cation-anion dual-site high-entropy doping strategy, which is designed to regulate the local chemical environment of O3-type layered oxide cathodes and enhance the covalency of TM-O bonds via the synergistic doping effects of multi-elements at cation sites (Li, Ti, Cu, Zn) and anion sites (F). The enhanced covalency of TM-O bonds can effectively simplify the phase transition process of O3-type layered oxide cathodes during the charge/discharge process and suppress the occurrence of irreversible phase transitions, thereby significantly improving the structural integrity of electrode materials. Furthermore, it can effectively inhibit the irreversible oxygen redox reactions and the dissolution of transition metal ions under high-voltage operating conditions. Benefiting from the aforementioned advantages, the designed O3-type $NaNi_{0.25}Fe_{0.14}Mn_{0.3}Li_{0.1}Ti_{0.15}Cu_{0.03}Zn_{0.03}O_{1.94}F_{0.06}$ (HEO) materials exhibit excellent cycling stability, favorable temperature tolerance, outstanding air stability, as well as superior full-cell performance, which fully verifies their potential for practical applications. The cation-anion dual-site high-entropy doping strategy proposed in this study provides a novel and universal paradigm for regulating the local chemical environment of O3-type layered oxide cathodes.

## Results and discussion

Conventional O3-type layered oxide cathodes suffer from adverse phase transitions, irreversible oxygen release, and transition metal ions dissolution during cycling (Fig. 1a). These issues further induce the formation of microcracks inside the material, impair its structural integrity, and ultimately lead to the degradation of electrochemical performance.[19] In general, the covalency of TM-O bonds is closely correlated with the structural stability of the O3-type layered oxide cathodes. Herein, a cation-anion dual-site high-entropy doping strategy is proposed to modulate the local chemical environment of O3-type layered oxide cathodes, thereby enhancing the covalency of TM-O bonds and ultimately achieving a breakthrough improvement in sodium storage performance. As shown in Fig. 1b, $Li^+$ with the $1s^2$ electron configuration and $Zn^{2+}$ with the $3d^{10}$ electron configuration are selected to enhance the local covalent bonding between Ni/Fe/Mn and O.[16,35] This enhancement is achieved through their weak hybridization with O 2p orbitals and the formation of Li/Zn-O-TM bridge-type structures.[36] $Ti^{4+}$ and $Cu^{2+}$ are selected due to their strong-bond-forming characteristics when bonding with O, which create non-positioned "rivets" within the structure and significantly enhance the local covalency of the bonding network.[19,37-38] Additionally, $F^-$ with a smaller ionic radius and higher electronegativity is doped into lattice oxygen sites. The formation of strong and short TM-F bonds leads to an overall contraction of the TM layer, thereby enhancing the orbital overlap between TM 3d and O 2p (Fig. S1, Supporting Information).[39-41] The strong TM-F bonds not only enhance structural stability but also, to some extent, influence the Na layer through the TM-F-Na bonding network (Fig. S2 and Table S1, Supporting Information).[42] This synergistic enhancement of TM-O covalency is expected to inhibit adverse phase transition processes, suppress irreversible $O_2$ release, restrain transition metal ions dissolution, and enhance structural stability under multiple application conditions.

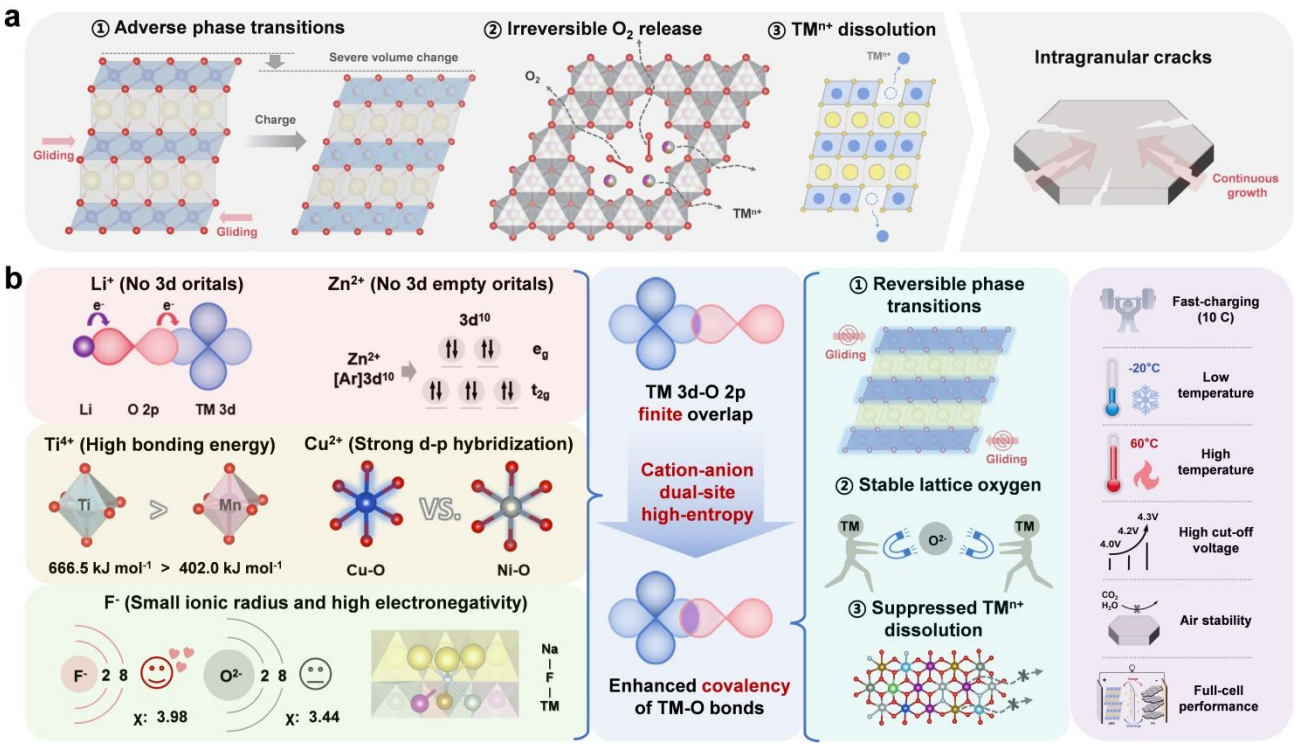


**Fig. 1.** (a) Challenges of O3-type layered oxide cathodes. (b) Schematic diagrams of cation-anion dual-site high-entropy doping strategy.

View Article Online
DOI: 10.1039/D6SC01783E





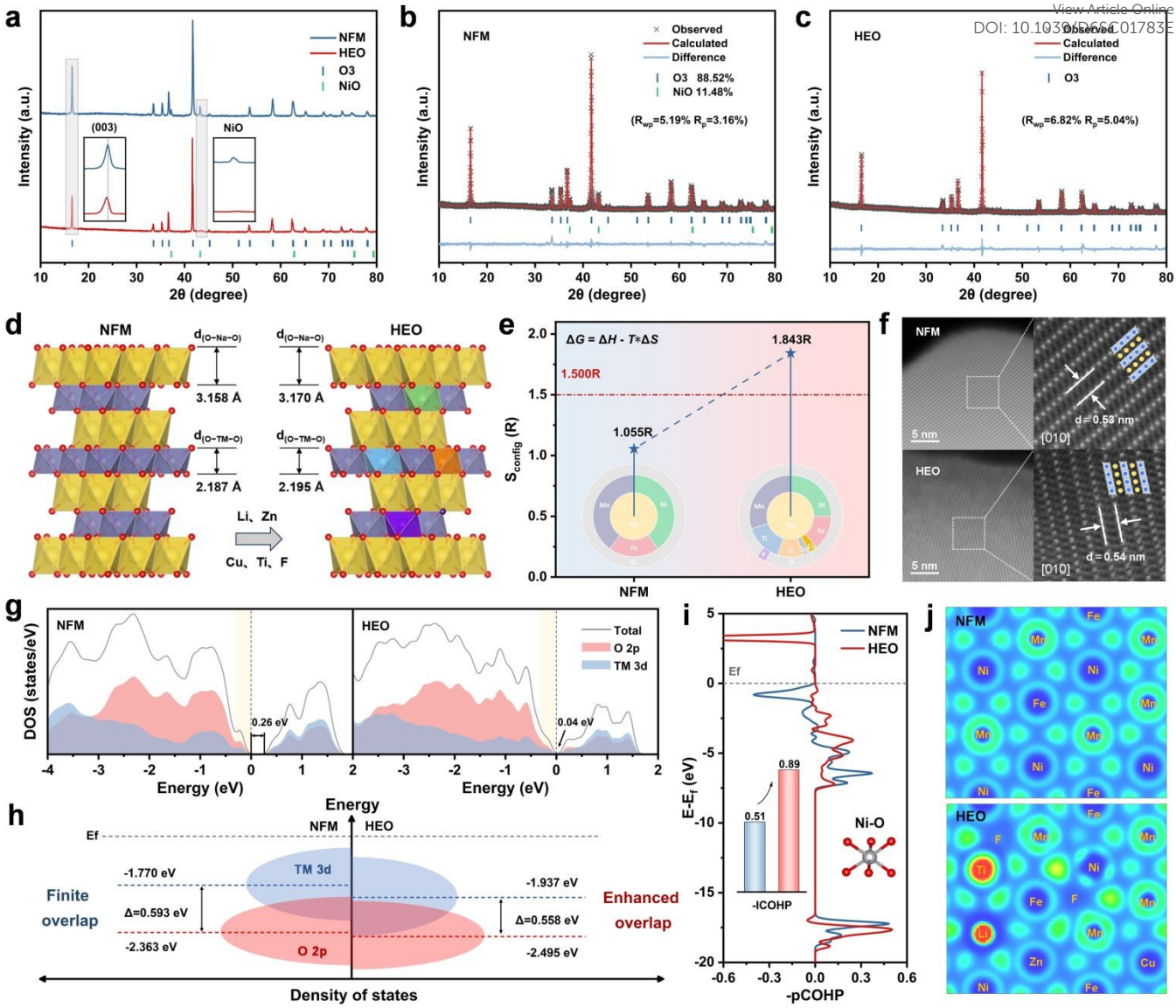


**Fig. 2.** (a) XRD patterns of NFM and HEO. Rietveld refinement results of (b) NFM and (c) HEO. Schematic diagrams of (d) crystal structure and (e) configurational entropy of NFM and HEO. (f) AC-HAADF-STEM images of NFM and HEO. (g) The density of states and (h) schematic diagrams of band structure of NFM and HEO. (i) COHP results of Ni-O bonds in NFM and HEO. (j) ELF of the valence electron in TM-layer viewed along the [001] direction.

To validate our design concept, $NaNi_{0.4}Fe_{0.2}Mn_{0.4}O_2$ (NFM) and $NaNi_{0.25}Fe_{0.14}Mn_{0.3}Li_{0.1}Ti_{0.15}Cu_{0.03}Zn_{0.03}O_{1.94}F_{0.06}$ (HEO) are synthesized via a simple solid-phase reaction. As shown in Fig. 2a, the sharp and distinct diffraction peaks indicate that both NFM and HEO can be classified as the O3-type structure (space group *R-3m*, PDF #88-0720). Additionally, the presence of NiO diffraction peaks (space group *Fm-3m*, PDF #47-1049) is observed in the XRD patterns of NFM, which is attributed to the solution limit of nickel in the O3 phase.[30] In contrast, HEO is a single-phase solid solution of O3-type. The detailed structural information for NFM and HEO is revealed via X-ray diffraction (XRD) Rietveld refinement (Fig. 2b-c and Table S2-S4). Compared to NFM, HEO exhibits an expanded d(O-Na-O) spacing (increased from 3.158 Å to 3.170 Å) and enlarged octahedral/tetrahedral volumes, which facilitates rapid $Na^+$ diffusion (Fig. 2d). Furthermore, the synergistic doping of multiple heterogeneous ions has led to a noticeable alteration in the d(O-TM-O) spacing. Subsequently, the elemental compositions were measured by inductively coupled plasma optical emission spectroscopy (ICP-OES) and fluoride-ion selective electrode method (ISE), and the results were in close accordance with the theoretically designed ratios (Table S5). As illustrated in Fig. 2e, co-doping with multiple heterogeneous ions induces a substantial increase in configurational entropy (from 1.055 R to 1.843 R), a signature that verifies the high-entropy nature of the HEO.[41,43]

The morphological and microstructural characterization of NFM and HEO were investigated by scanning electron microscopy (SEM) and transmission electron microscopy (TEM). As shown in Fig. S3 (Supporting Information), NFM and HEO

View Article Online
DOI: 10.1039/D6SC01787F



exhibit similar primary particles with clean surfaces and average particle sizes of about 1 μm. High-resolution transmission electron microscopy (HRTEM) images reveal that both HEO and NFM exhibit the characteristic (003) lattice fringes of O3 phase, with HEO displaying a larger interplanar spacing (Fig. S4, Supporting Information).[14] By spherical aberration corrected scanning transmission electron microscope (AC-STEM) combined with high-angle annular dark-field (HAADF) imaging (Fig. 2f and Fig. S5, Supporting Information), an increased interplanar spacing (5.4 Å vs. 5.3 Å) is further confirmed in the HEO, which is consistent with the increase of the lattice parameter *c*. Furthermore, energy dispersive spectroscopy (EDS) elemental mappings confirm the uniform distribution of each element throughout the bulk phase in NFM and HEO (Fig. S6 and Fig. S7, Supporting Information).

In general, the stability of the bonds between TM and O are closely related to the sodium storage performance of O3-type layered oxide cathode materials. X-ray absorption near-edge structure (XANES) spectra and Fourier-transformed extended X-ray absorption fine structure (FT-EXAFS) techniques are first employed to reveal the electronic structure and coordination information of transition metal ions in NFM and HEO (Fig. S8 and Fig. S9, Supporting Information).[44] The initial oxidation states of Ni, Fe, and Mn in both materials are +2, +3, and +4, respectively. Noticeably, the Ni-O, Fe-O, and Mn-O bonds in the HEO all exhibit significant shortening, indicating that higher bonding energies enhance structural stability. This sufficiently robust covalent bonding network will significantly improve the sodium storage performance.[20] Subsequently, density functional theory calculations (DFT) are employed to elucidate the impact of cation-anion dual-site high-entropy doping strategy on the electronic structure. The total density of states (TDOS) in Fig. 2g reveals a markedly narrower band gap near the Fermi level after modification (as marked by the black arrow), indicating enhanced electronic conductivity.[45] As shown in Fig. 2h, the O 2p band center shifted downward in HEO, which implies an increase of the stabilization of the oxygen redox reaction.[32,46] Concurrently, the energy difference between the TM 3d and O 2p band center was decreased (0.593 eV vs. 0.558 eV), corresponding to strengthened hybridization of the TM 3d-O 2p orbitals. Collectively, these results confirm that the cation-anion dual-site high-entropy doping strategy enhances the covalency of TM-O bonds, thereby fortifying the structural stability of the cathode material.[10,47] Furthermore, the Li 2s and Zn 3d orbitals exhibit negligible hybridization with O 2p orbitals near the Fermi level, which is consistent with the design expectations based on our element selection strategy (Fig. S10, Supporting Information). The changes in TM-O bonding energies were further quantified by crystal orbital Hamilton population (COHP) analyses Fig. 2i and Fig. S11, Supporting Information). Compared to NFM, Ni/Fe/Mn-O bonds in HEO exhibit higher -ICOHP values, with more bonding filling orbitals and anti-bonding empty orbitals. This observation indicates that the proposed doping strategy can effectively enhance the covalency of TM-O bonds.[21,48-50] Subsequently, the electronic localization function (ELF) was employed to characterize the degree of charge localization around the constituent ions within the crystal structure (Fig. 2j). The localized charges on the O and TM atoms are more delocalized in HEO, indicating stronger interactions between TM and O. Moreover, the weak hybridization phenomenon in Li/Zn-O ionic bonds and unique Li/Zn-O-TM bridge-type charge-transfer structures observed in HEO, aligns with the findings reported in previous literature.[16,36] As illustrated in Fig. S12 and Fig. S13 (Supporting Information), the local coordination environment constructed by the strong-bond-forming ions (Ti, Cu, and F) anchored within the TM layer plays a pivotal role in enhancing the overall covalency of the material system. These results demonstrate that the cation-anion dual-site high-entropy doping strategy effectively modulates the local covalency of the material, thereby enhancing its structural stability and ultimately achieving excellent sodium storage performance.[20]

To validate the superiority of the cation-anion dual-site high-entropy doping strategy, we evaluated the sodium storage performance of NFM and HEO using half-cells. As shown in Fig. 3a, the cyclic voltammetry (CV) curves of the two materials exhibit significant differences. On the one hand, NFM shows redox peaks at approximately 3.4 V due to $Na^+$/vacancy ordering, a process that reduces structural stability and hinders $Na^+$ diffusion, whereas this phenomenon is absent in HEO.[30] On the other hand, in the high-voltage range of 4.0-4.2 V, NFM presents sharp and asymmetric redox peaks, in stark contrast to the smooth and symmetric peaks of HEO. This collectively demonstrates that HEO effectively suppresses $Na^+$/vacancy ordering, as well as severe phase transitions and irreversible oxygen reactions at high voltages. The galvanostatic charge/discharge curves in Fig. 3b further validate the positive role of the cation-anion dual-site high-entropy doping strategy in suppressing irreversible phase transitions and limiting oxygen redox reactions. In addition, HEO shows an accepted reversible capacity of 152.27 mAh $g^{-1}$ with higher initial Coulombic efficiency of 98.71%. As shown in Fig. 3c-d and Fig. S14 (Supporting Information), HEO demonstrates superior rate performance compared to NFM, with reversible capacities of 150.18, 145.64, 141.21, 126.75, 115.98, 98.01 mAh $g^{-1}$ at 0.2, 0.5, 1.0, 5.0, 10.0, 20.0 C, respectively. HEO exhibits a middle voltage of 3.205 V, energy density of 482.3 Wh $kg^{-1}$ and power density of 100.69 W $kg^{-1}$ at 0.2 C (Fig. S15, Supporting Information). Even at a high current density of 20.0 C, its performance remains outstanding, achieving 2.707 V, 268.1 Wh $kg^{-1}$, and 8.94 kW $kg^{-1}$, respectively. Meanwhile, HEO demonstrates excellent long-term cycling stability and delivers a high capacity retention of 73.69% with a reversible capacity of 95.57 mAh $g^{-1}$ after 500 cycles at 10.0 C (Fig. 3e). In contrast, NFM exhibits significant capacity degradation, and the battery fails completely after 150 cycles. It is noteworthy that the cycling stability of HEO is comprehensively superior to that of NFM at various current densities and cut-off voltage (Fig. S16-S20, Supporting Information).

Subsequently, we further investigated the effect of the cation-anion dual-site high-entropy doping strategy on the temperature tolerance of O3-type layered oxide cathode materials. As the operating temperature decreased (-20 °C), the reversible capacities

View Article Online
DOI: 10.1039/D5SC01787D



of both electrode materials declined with HEO exhibiting significantly higher capacity retention than NFM (75.16% vs. 69.28%, Fig. S21, Supporting Information). As shown in Fig. 3f-g, and Fig. S22 (Supporting Information), HEO demonstrated superior rate performance and cycling stability compared to NFM, delivering a high reversible capacity of 85.90 mAh $g^{-1}$ at 4.0 C and a high capacity retention of 90% after 200 cycles. When the operating temperature was raised to 60 °C, NFM suffered from severe side reactions, leading to poor sodium storage performance (Fig. 3h-i and Fig. S23-S24, Supporting Information).[51] In contrast, HEO exhibited excellent rate performance (107.30 mAh $g^{-1}$ at 20.0 C) and outstanding cycling stability (capacity retention of 63.77% after 300 cycles). Compared with advanced O3-type layered oxide cathodes reported in the past three years, the HEO developed in this work achieves a balance among reversible capacity, cycling stability, rate performance, and temperature tolerance. Its comprehensive electrochemical performance significantly surpasses that of previously reported counterparts (Fig. 3j, Fig. S25, and Table S6-S7, Supporting Information).

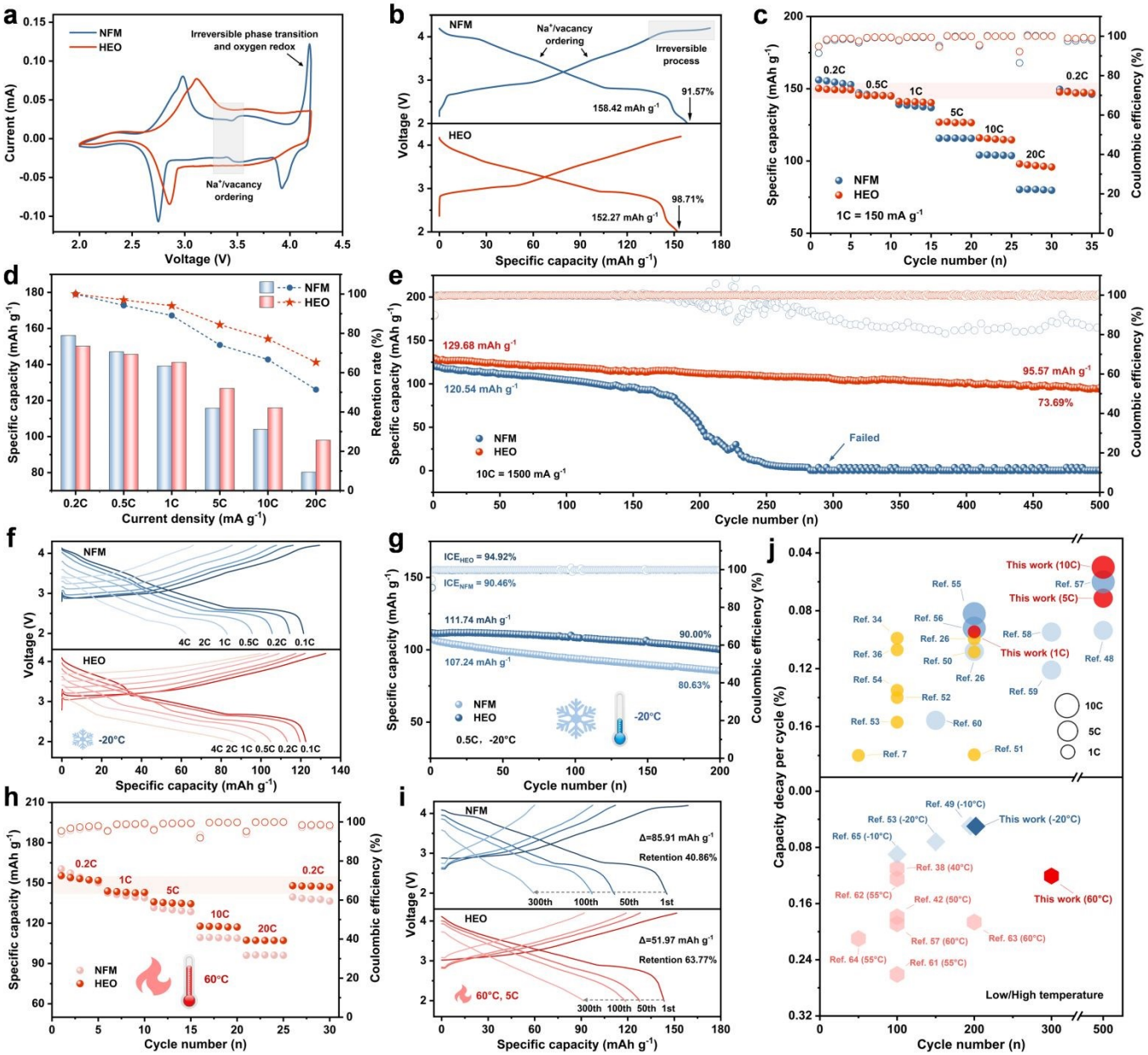


**Fig. 3.** (a) CV curves of NFM and HEO at 0.1 mV $s^{-1}$ for the first cycle. (b) Initial galvanostatic charge/discharge curves of NFM and HEO at 0.1 C (1 C = 150 mA $g^{-1}$). (c) Rate performance of NFM and HEO. (d) Specific capacity comparison between NFM and HEO at different current densities. (e) Long-term cycling performance at 10.0 C. (f) Rate performance and (g) cycling performance at -20 °C low temperature. (h) Rate performance and (i) cycling performance at 60 °C high temperature. (j) Comparison of half-cell performance with reported literatures over the past three years.[7,26,34,36,38,44,50-67]

To elucidate the origin of the enhanced electrochemical performance, we first systematically investigated the charge transfer kinetics. Based on the linear fitting results between the square root of the scanning rate ($v^{1/2}$) and the corresponding

View Article Online
DOI: 10.1039/D6SC01783F

peak current, the $Na^+$ diffusion kinetics of HEO are significantly improved compared to those of NFM (Fig. S26, Supporting Information). This conclusion was further validated by the galvanostatic intermittent titration technique (GITT) analysis: HEO exhibits a higher average $Na^+$ diffusion coefficient during charge/discharge process, especially within the high-voltage range of 4.0-4.2 V (Fig. S27, Supporting Information). Meanwhile, the more continuous and smaller variations in the $Na^+$ diffusion coefficient indirectly reflect the milder phase transitions in HEO. Moreover, electrochemical impedance spectroscopy (EIS) results show that the impedance values of HEO during the cycling process are also lower than those of NFM, indicating fast charge transfer in HEO (Fig. S28, Supporting Information). These findings collectively highlight the positive role of cation-anion dual-site high-entropy doping strategy in enhancing the electrochemical reaction kinetics, which is responsible for the improved rate performance.

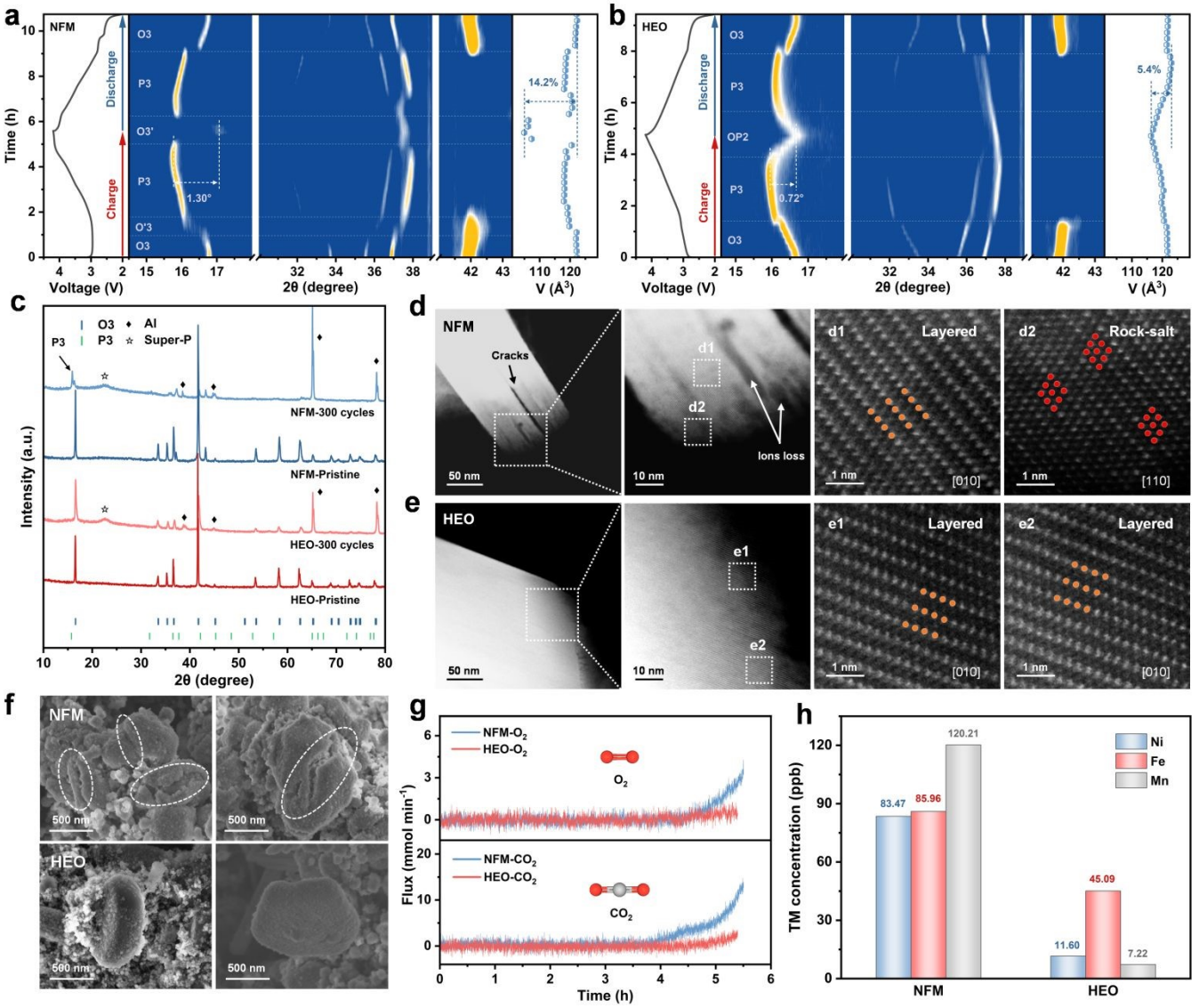


**Fig. 4.** *In-situ* XRD contour maps and the corresponding lattice volume changes of (a) NFM and (b) HEO during the first cycle at 0.2 C. (c) XRD patterns before and after 300 cycles. (d-e) AC-HAADF-STEM images and (f) SEM images of NFM and HEO after 300 cycles. (g) Comparison of *in-situ* DEMS results for the first charge to 4.2 V. (h) Concentrations of deposited transition metal ions in NFM||Na and HEO||Na after 300 cycles.

*In-situ* X-ray diffraction (XRD) is employed to monitor the structural evolution of NFM and HEO during the initial charge/discharge process (Fig. 4a-b and Fig. S29-S30, Supporting Information). During the initial charge process, both NFM and HEO show consistent variations in their characteristic diffraction peaks. As $Na^+$ extraction enhances the interlayer $O^{2-}$-$O^{2-}$ electrostatic repulsion and leads to *c*-axis expansion, the $(003)_{O3}$ peaks shift toward lower angles. Concurrently, the shifts of the $(101)_{O3}$ and $(012)_{O3}$ peaks toward higher angles corresponds to contraction of the *ab*-plane, which is attributed to the progressive oxidation of active transition metal ions. Subsequently, an O'3 phase (monoclinic, C2/m) distinct from the O3 phase is observed in NFM. This phase is typically associated with collective Jahn-Teller distortion of $Ni^{3+}$, which

View Article Online
DOI: 10.1039/D5SC01787F



exacerbates lattice distortion and compromises structural stability.[36,41,49] Noticeably, HEO in the same stage maintains a solid solution reaction of the O3 phase. The absence of the O'3 phase indicates that Jahn-Teller distortion is effectively mitigated, benefiting from the expanded $TMO_2$ slabs and a robust TM-O bonding environment.[30,68] Subsequently, the appearance of the $(003)_{P3}$ peaks in NFM and HEO confirms the phase transformation to the P3 phase, with the solid solution reactions (accompanied by minor variations in unit cell parameters) proceeding continuously. When the voltage exceeds 4.0 V, NFM and HEO undergo distinct phase transitions: NFM rapidly transforms from the P3 phase to the Na-deficient O3' phase (hexagonal, similar to the pristine O3 structure), which induces severe lattice distortion and a propensity for irreversible lattice oxygen loss and transition metal ions dissolution.[7] In contrast, HEO undergoes a gradual evolution into the highly reversible OP2 phase.[41,69] Lattice parameters and volume changes during initial charge/discharge were further obtained from *in-situ* XRD patterns Rietveld refinement (Fig. S31, Supporting Information). NFM exhibits an abrupt 14.2% maximum volume change, triggering stress concentration and crack propagation, while HEO undergoes a gentle 5.4% variation to maintain particle integrity. In summary, the anchored TM layer constructed by the cation-anion dual-site high-entropy doping strategy enables a highly reversible O3→P3→OP2 phase transition. It efficiently suppresses Jahn-Teller distortion and the unfavorable O3' phase, thereby significantly improving cycling stability (Fig. S32, Supporting Information).

The effect of cation-anion dual-site high-entropy doping strategy on structural stability during long-term cycling is further revealed by XRD, SEM, TEM, and AC-STEM. As illustrated in Fig. 4c and Fig. S33 (Supporting Information), the NFM exhibits residual P3 phase peaks after 300 cycles, indicative of irreversible phase transitions within the material. In sharp contrast, HEO maintains a pure O3 phase structure, testifying to its exceptional structural stability that underpins enhanced cycling longevity. Subsequently, atomic-resolution AC-HAADF-STEM images in Fig. 4d and Fig. 4e reveal the detailed structural information of the cathode materials after cycling. Specifically, the HEO cathode preserves a well-defined layered architecture, free of discernible cracking or substantial phase transformations. Evidently, the maximal retention of the pristine structure constitutes the critical structural basis for the long-term cycling stability of HEO.[69] However, the NFM cathode suffers from prominent cracking, with extensive rock-salt phase formation at the fracture sites; meanwhile, severe surface reconstruction synergistically undermines its structural integrity.[13,70] As observed from the SEM and TEM images, the surfaces of NFM particles are covered with numerous cracks, accompanied by severe particle fragmentation (Fig. 4f and Fig. S34, Supporting Information). In stark contrast, the HEO particles retain their structural integrity after cycling.[12] Furthermore, TEM images clearly demonstrate that a uniform and dense cathode electrolyte interphase (CEI) layer is formed on the surface of HEO. This interfacial layer effectively suppresses the interfacial side reactions and the transition metal ions dissolution, thereby significantly enhancing the sodium storage performance of HEO. The real-time release behavior of $O_2$ (m/z = 32) and $CO_2$ (m/z = 44) during the initial charge process is probed by *in-situ* differential electrochemical mass spectrometry (DEMS, Fig. 4g).[71] Compared to NFM, HEO exhibits significantly reduction in the release of $O_2$ and $CO_2$ during the process, demonstrating that irreversible $O_2$ release and interfacial side reactions are effectively suppressed. Additionally, inductively coupled plasma optical emission spectrometry (ICP-OES) measurements reveal that the dissolution of Ni, Fe, and Mn from HEO is significantly lower than that from NFM (Fig. 4h).[41] This observation indicates that the robust TM-O bonds exhibit excellent stability during charge/discharge process, which effectively suppresses transition metal ions dissolution, preserves active redox sites, and mitigates structural degradation. Collectively, these findings underscore the favorable effect of the cation-anion dual-site high-entropy doping strategy on reinforcing the covalency of TM-O bonds, a key contributor to the enhanced cycling performance.

*Ex-situ* X-ray photoelectron spectroscopy (XPS) and X-ray absorption spectroscopy (XAS) are employed to elucidate the charge compensation mechanisms in NFM and HEO. The Ni 2p and Fe 2p XPS spectra of the two materials exhibit similar peak shifts during charge/discharge process (Fig. 5a-c and Fig. S35, Supporting Information). As electrochemically active elements, Ni and Fe contribute to the capacity via electron transfer and valence state variations, following the redox pathways of $Ni^{2+}$→$Ni^{4+}$ and $Fe^{3+}$→$Fe^{4+}$. In contrast, no significant peak shifts were observed for Mn in NFM, nor for Mn, Li, Ti, Cu, and Zn in HEO in the XPS spectra, indicating that these elements act as electrochemically inert species to stabilize the host structure (Fig. S36, Supporting Information). Upon charging to 4.2 V, a new characteristic peak at approximately 530.5 eV (assigned to $(O_2)^{n-}$ species) emerged in the O 1s XPS spectra of both materials (Fig. 5d). Notably, the signal intensity in NFM was distinctly higher than that in HEO, which is consistent with the electron paramagnetic resonance (EPR) measurements, indicating that more pronounced oxygen redox reactions occurred in NFM (Fig. S37, Supporting Information).[21,34,38] Furthermore, obvious disparities between the two materials were observed after discharging to 2.0 V: the characteristic peak of $(O_2)^{n-}$ species almost completely vanished in HEO, testifying to the highly reversible nature of its oxygen redox reactions; by contrast, partial $(O_2)^{n-}$ species was detected in NFM, revealing the poor reversibility of oxygen redox reactions.[64,72] This phenomenon is further confirmed by the Raman spectroscopy results (Fig. S38, Supporting Information).[41,73] These results demonstrate the superior lattice oxygen stability and controllable redox activity of HEO, which in turn ensures excellent structural stability throughout charge/discharge cycling. Normalized X-ray absorption near-edge structure (XANES) spectra of the Ni, Fe, and Mn K-edges are shown in Fig. 5e-g and Fig. S39 (Supporting Information). For both NFM and HEO, the Ni and Fe K-edge XANES spectra exhibited pronounced shifts during charging and reversibly reverted to their initial positions upon discharging, further

View Article Online
DOI: 10.1039/D5SC01785E

demonstrating the key role of Ni and Fe as electrochemically active elements in the charge compensation mechanism.[36] Meanwhile, Mn retained a consistent +4 oxidation state throughout the process, with negligible shifts in its K-edge XANES profile, thus further verifying its electrochemical inertness as a structural framework component.[71] Fourier-transformed extended X-ray absorption fine structure (FT-EXAFS) spectra of the two materials in different states offer profound insights into the evolution of local structures during charge/discharge process (Fig. 5h-j and Fig. S40-S41, Supporting Information). The first coordination shell corresponds to Ni/Fe/Mn-O bonds. During charging, the Ni/Fe-O bond length shortens markedly, accompanied by continuous contraction of the $TMO_6$ octahedral structure, a phenomenon closely correlated with the progressive oxidation of the electrochemically active Ni/Fe sites. In contrast, the negligible shifts in the Mn-O bond signals confirm the stable +4 oxidation state of Mn throughout the process.[34,65,71]

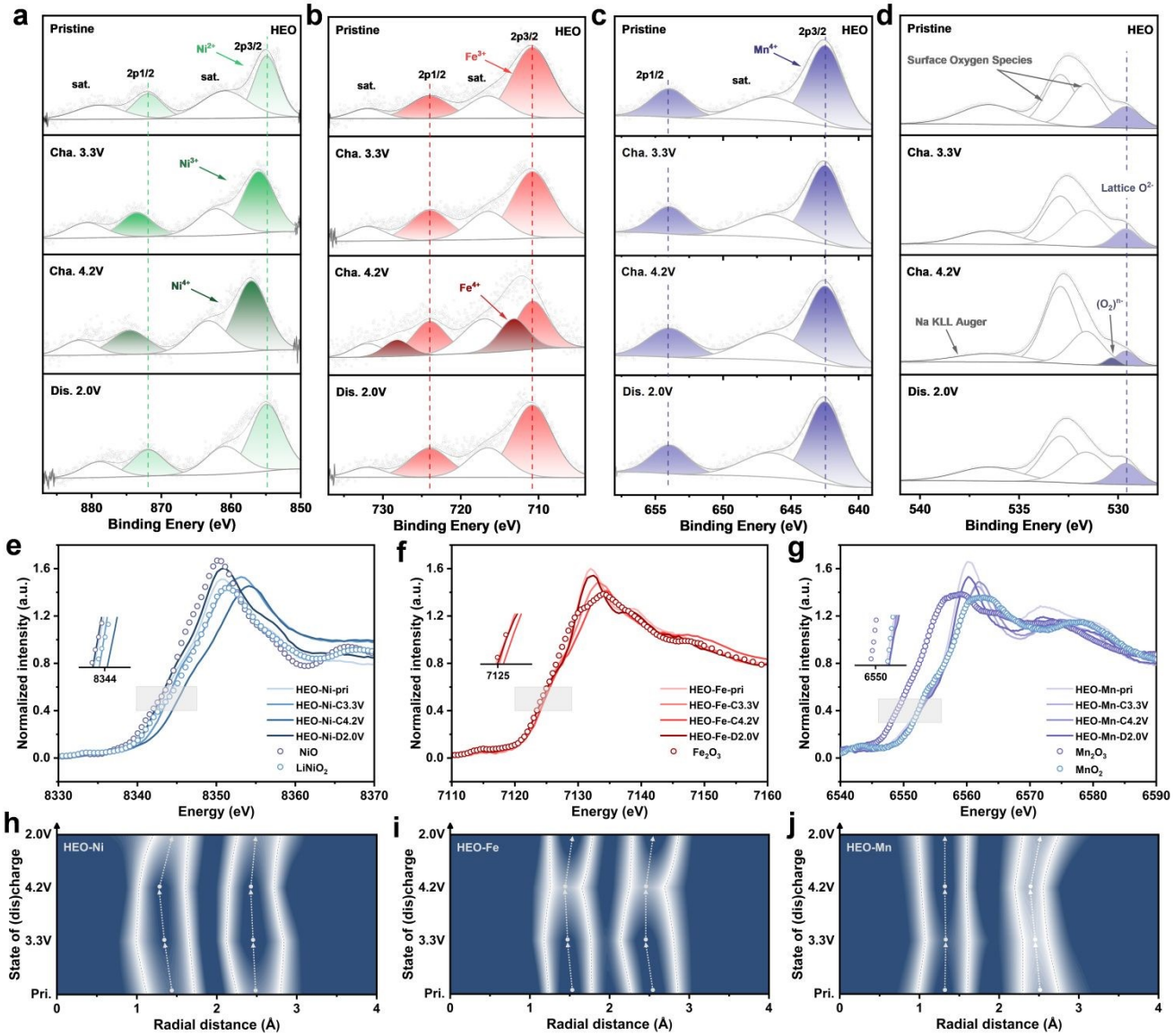


**Fig. 5.** XPS spectra of (a) Ni 2p, (b) Fe 2p, (c) Mn 2p, and (d) O 1s in HEO at various charge/discharge states during the initial cycle. XANES spectra of (e) Ni-K-edge, (f) Fe K-edge, and (g) Mn K-edge of HEO. Contour maps of (h) Ni, (i) Fe, and (j) Mn K-edge FT-EXAFS spectra of HEO.

The air stability and full-cell performance of O3-type layered oxide cathode materials exert a decisive influence on their prospects for commercial application.[4,27] The phase structure evolution of NFM and HEO powders upon prolonged exposure to ambient air with a relative humidity of about 70% was first investigated by XRD (Fig. 6a and Fig. 6b). After 7 days of air exposure, characteristic diffraction peaks corresponding to $Na_2CO_3{\cdot}nH_2O$, the monoclinic O3 phase, and the hydration phase emerged in the NFM, indicating that effective sodium continuously leaches out, accompanied by structural distortion and further $H_2O$ insertion.[74] When the air exposure duration extends to 10 days, the characteristic peaks of the undesired byproducts become more pronounced. Meanwhile, the $(003)_{O3}$ diffraction peak exhibits a significant shift relative to the pristine

View Article Online
DOI: 10.1039/D5SC01785E



sample, signifying substantial alterations in the interlayer spacing of the layered structure. In stark contrast, the HEO with regulated local chemistry maintains a highly crystalline, with negligible shifts in its characteristic peaks even after 10 days of exposure to such high-humidity air (Fig. S42, Supporting Information).[57] In addition, HEO also exhibits minimal capacity degradation, excellent rate performance, and remarkable cycling stability after prolonged air exposure (Fig. 6c-e and Fig. S43-S44, Supporting Information). These observations explicitly verify that the enhanced local covalency of the material, imparted by the cation-anion dual-site high-entropy doping strategy, can effectively elevate the air stability of O3-type layered oxide cathode materials. Subsequently, full cells were assembled using hard carbon anodes to systematically evaluate the electrochemical performance of HEO (Fig. 6f and Fig. 6g). As illustrated in Fig. 6h and Fig. S45 (Supporting Information), the HEO||HC full cell displays excellent rate performance, delivering high reversible capacities of 138.31, 124.11, 114.58, 107.28, 99.93 mAh $g^{-1}$ at current densities of 10, 20, 50, 100, 200 A $g^{-1}$, respectively. At a current density of 50 mA $g^{-1}$, the HEO||HC full cell achieves a favorable energy density of 252.35 Wh $kg^{-1}$, calculated based on the combined mass of the cathode and anode. More importantly, the HEO||HC full cell demonstrates outstanding cycling stability, maintaining a high capacity retention of 70.35% after 500 cycles (Fig. 6i-j). Moreover, the HEO||HC full cells exhibit high discharge capacity and excellent cycling stability over a wide voltage range (Fig. S46, Supporting Information). These results demonstrate that the HEO with regulated local chemistry exhibits considerable potential for practical applications.

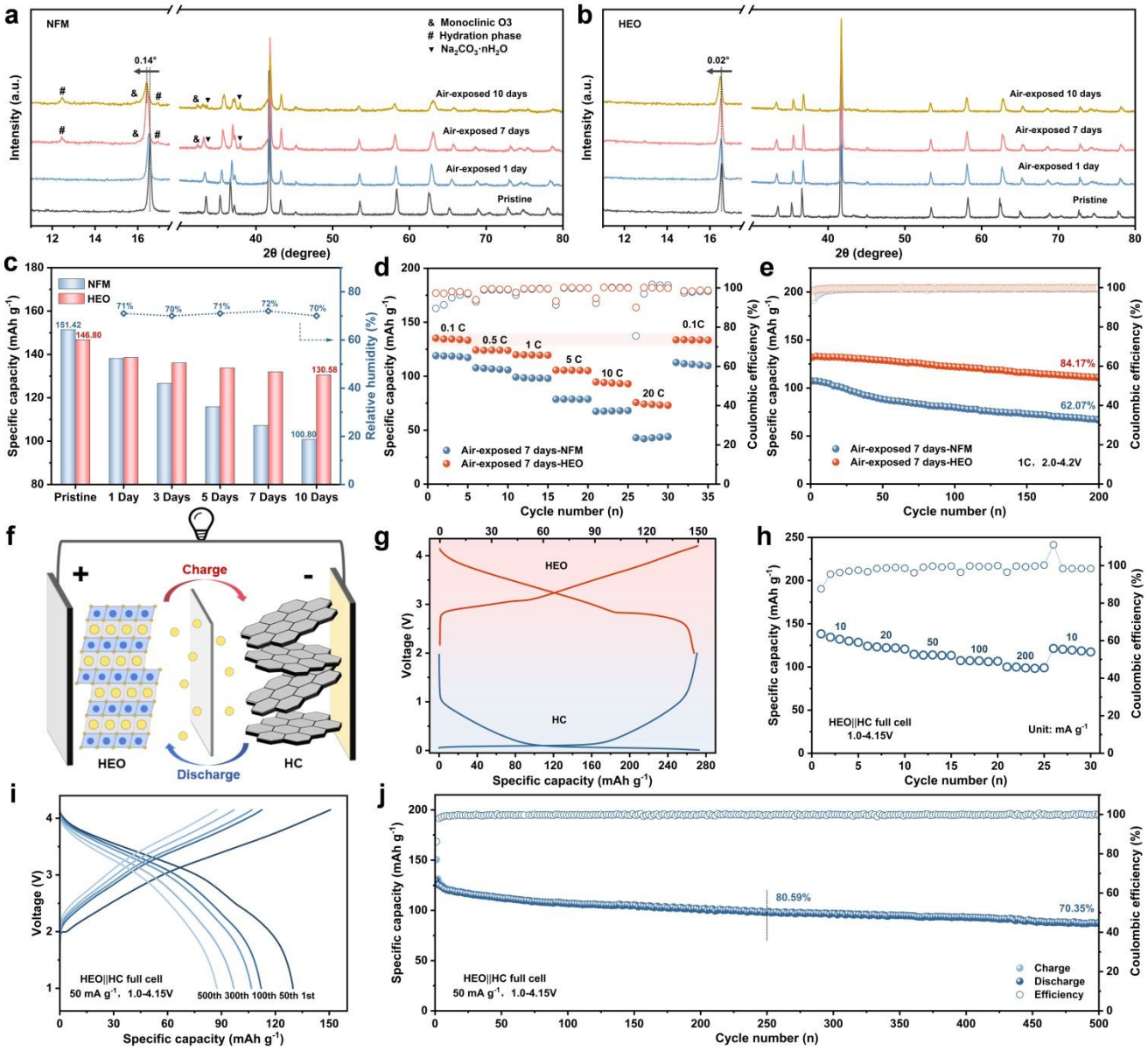


**Fig. 6.** XRD patterns of (a) NFM and (b) HEO before and after air exposure. Comparison of (c) specific capacity, (d) rate performance, (e) cycling performance of NFM and HEO exposed to air. (f) Schematic diagram of the HEO||HC full cell. (g) Initial galvanostatic

charge/discharge curves of HEO cathode and HC anode after precycled. (h) Rate performance and (i-j) long-term cycling performance of the HEO||HC full cell.

View Article Online
DOI: 10.1039/D6SC01783E

## Conclusions

In summary, this work proposes a cation-anion dual-site high-entropy doping strategy to modulate the local chemical environment of O3-type layered oxide cathode materials, thereby achieving a remarkable enhancement in their sodium storage performance. Specifically, the introduction of Li, Ti, Cu and Zn at cation sites, combined with F doping at anion sites, synergistically strengthens the covalency of the TM-O bonds. This dual-site synergistic modulation effect exhibits prominent advantages: i) the strongly covalent TM-O bonds can effectively suppress the undesirable phase transitions during the charge/discharge process, thus preserving the integrity of the electrode material; ii) it significantly inhibits the occurrence of irreversible oxygen redox reactions, reduces oxygen loss, and simultaneously mitigates the dissolution of transition metal ions, fundamentally improving the long-term cycling stability of the material. As a result, the designed HEO not only delivers a high specific capacity of 152.27 mAh $g^{-1}$, but also achieves an excellent capacity retention of 73.69% after 500 cycles. More importantly, this material also possesses outstanding temperature tolerance, favorable air stability and reliable full-cell performance, highlighting its enormous application potential in the practical implementation of SIBs. The cation-anion dual-site high-entropy doping strategy developed in this work features excellent universality and scalability and provides an efficient approach for regulating the local chemical environment of O3-type layered oxide cathodes. Moreover, the simultaneous doping at both TM and O sites enriches the design theory of high-entropy cathode materials for advanced sodium-ion batteries.

## Author contributions

L. L., K. L., and S. Z. obtained the funds and supervised the project; T. H. and K. L. conceived the idea; T. H., Q. Y., and G. Y. designed the experiments; T. H., Q. Y., G. Y., M. L., X. B., T. L., X. Z., and J. X. performed experiments; T. H., K. L., X. Z., and X. T. analyzed the data; and T. H. wrote the original manuscript. All authors revised and approved the manuscript.

## Conflicts of interest

There are no conflicts to declare.

## Acknowledgements

This work was funded by the National Natural Science Foundation of China (52202286, 22309002), Key Research and Development Program of Zhejiang Province (2024C01057), Natural Science Foundation of Hebei Province (E2024202239, B2024202081), Science and Technology Plan Project of Wenzhou Municipality (ZG2024055), Science Research Project of Hebei Education Department (CXY2024036), the Tianjin Science and Technology Plan Project (24JCQNJC00750), China National Postdoctoral Program for Innovative Talents (BX20250118). We would like to thank Advanced Materials Testing and Analysis Center of Hebei University of Technology. The authors extend their gratitude to Scientific Compass (www.shiyanjia.com) for providing invaluable assistance for EPR.

## Notes and references

1 Q. Liu, Z. Hu, W. Li, C. Zou, H. Jin, S. Wang, S. Chou, S. Dou, *Energy Environ. Sci.* 2021, **14**, 158-179.
2 J. Ren, H. Zhu, Y. Fang, W. Li, S. Lan, S. Wei, Z. Yin, Y. Tang, Y. Ren, Q. Liu, *Carbon Neutralization* 2023, **2**, 339-377.
3 H. Kim, J. Kim, *eScience* 2024, **4**, 100232.
4 F. Li, W. Tang, J. Wu, L. Zhang, A. Mu, Z. Chen, *Adv. Energy Mater.* 2024, **14**, 2401564.
5 Y. Gao, H. Zhang, J. Peng, L. Li, Y. Xiao, L. Li, Y. Liu, Y. Qiao, S. Chou, *Carbon Energy* 2024, **6**, e464.
6 Z. Chen, Y. Deng, J. Kong, W. Fu, C. Liu, T. Jin, L. Jiao, *Adv. Mater.* 2024, **36**, 2402008.
7 N. Hong, J. Li, H. Wang, X. Hu, B. Zhao, F. Hua, Y. Mei, J. Huang, B. Zhang, W. Jian, J. Gao, Y. Tian, X. Shi, W. Deng, G. Zou, H. Hou, Z. Hu, Z. Long, X. Ji, *Adv. Funct. Mater.* 2024, **34**, 2402398.
8 X. Zhang, Q. Yang, J. Xu, T. Lv, M. Li, G. Yu, T. Huo, X. Zhou, X. Bai, L. Li, K. Lei, *Chin. Chem. Lett.* 2025, DOI: 10.1016/j.cclet.2025.112268.
9 D. Eum, B. Kim, J. Song, H. Park, H. Jang, S. Kim, S. Cho, M. Lee, J. Heo, J. Park, Y. Ko, S. Park, J. Kim, K. Oh, D. Kim, S. Kang, K. Kang, *Nat. Mater.* 2022, **21**, 664-672.
10 S. Thekkekara, P. Tripathi, J. Sudharma, P. Anurag, V. Srihari, H. Poswal, A. Singh, M. Shaijumon, *Small* 2025, **21**, 2502341.
11 M. Gu, J. Xu, X. Shi, L. Shao, Z. Sun, *Battery Energy* 2024, **3**, 20230046.
12 Y. Bi, J. Tao, Y. Wu, L. Li, Y. Xu, E. Hu, B. Wu, J. Hu, C. Wang, J. Zhang, Y. Qi, J. Xiao, *Science* 2020, **370**, 1313-1317.
13 J. Li, H. Yang, Q. Deng, W. Li, Q. Zhang, Z. Zhang, Y. Chu, C. Yang, *Angew. Chem. Int. Ed.* 2024, **63**, e202318042.
14 J. Wu, W. Zhou, S. Zhang, J. Wang, J. Dong, C. Ma, K. Zhang, Y. Lu, Z. Yan, M. Song, J. Chen, *Angew. Chem. Int. Ed.* 2025, **64**, e202519551.
15 X. Ou, T. Liu, W. Zhong, X. Fan, X. Guo, X. Huang, L. Cao, J. Hu, B. Zhang, Y. Chu, G. Hu, Z. Lin, M. Dahbi, J. Alami, K. Amine, C. Yang, J. Lu, *Nat. Commun.* 2022, **13**, 2319.
16 Z. Wang, R. Hu, H. Chen, Y. Ye, Q. Zhao, Z. Du, S. Yang, *Energy Environ. Sci.* 2025, **18**, 6832-6840.
17 Y. Sun, J. Weng, P. Zhou, W. Yuan, Y. Pan, X. Wu, J. Zhou, F. Cheng, *Adv. Mater.* 2024, **36**, 2410575.
18 M. Sun, Z. Liu, L. Liu, Y. Zheng, S. Lv, N. Zhang, L. Deng, L. Zhao, Z. Wang, *Adv. Energy Mater.* 2025, **15**, e03154.
19 X. Cai, Z. Shadike, N. Wang, X. Li, Y. Wang, Q. Zheng, Y. Zhang, W. Lin, L. Li, L. Chen, S. Shen, E. Hu, Y. Zhou, J. Zhang, *J. Am. Chem. Soc.* 2025, **147**, 5860-5870.
20 Q. Lai, H. Yue, D. Yang, G. Gao, H. Chen, X. Gao, Z. Liu, Q. Gu, W. Luo, *Adv. Energy Mater.* 2025, DOI: 10.1002/aenm.202504890.
21 H. Lu, S. Chu, J. Tian, Q. Wang, C. Sheng, C. Cheng, R. Liu, A. D'Angelo, W. K. Pang, L. Zhang, H. Zhou, S. Guo, *Adv. Funct. Mater.* 2024, **34**, 2305470.
22 Q. Lai, C. Liu, D. Yang, X. Gao, R. Yang, Q. Li, Z. Liu, Q. Gu, W. Luo, *Adv. Funct. Mater.* 2025, DOI: 10.1002/adfm.202516173.
23 C. Cheng, Y. Shen, C. Chen, S. Tang, Z. Zhuo, Q. Niu, C. Yuan, T. Chen, L. Wang, J. Guo, D. Sun, L. Zhang, *Adv. Energy Mater.* 2025, **15**, e04261.
24 E. Gabriel, C. Ma, K. Graff, A. Conrado, D. Hou, H. Xiong, *eScience* 2023, **3**, 100139.

25 H. Wang, L. Li, W. Han, H. Guo, A. BobrikovIvan, Y. Chai, X. Liu, *Renewables* 2023, **1**, 253-265.
26 J. Yao, X. Wang, P. Hu, J. Fan, X. Yang, W. Jiang, S. Jiang, P. Dong, Y. Zhang, J. Duan, Z. Zhou, *Adv. Funct. Mater.* 2024, DOI: 10.1002/adfm.202419967.
27 L. Duan, Y. Zhang, H. Tang, J. Liao, G. Zhou, X. Zhou, *Adv. Mater.* 2025, **37**, 2411426.
28 L. He, T. Feng, Q. Wu, Y. Cao, F. Song, *Rare Metals* 2025, **44**, 5355-5369.
29 K. Zhang, Z. Xu, G. Li, R. Luo, C. Ma, Y. Wang, Y. Zhou, Y. Xia, *Adv. Energy Mater.* 2023, **13**, 2302793.
30 F. Ding, C. Zhao, D. Xiao, X. Rong, H. Wang, Y. Li, Y. Yang, Y. Lu, Y. Hu, *J. Am. Chem. Soc.* 2022, **144**, 8286-8295.
31 B. Wang, J. Ma, K. Wang, D. Wang, G. Xu, X. Wang, Z. Hu, C. Pao, J. Chen, L. Du, X. Du, G. Cui, *Adv. Energy Mater.* 2024, **14**, 2470094.
32 Z. Li, W. Xi, Z. Jiang, Y. Zhang, R. Wang, Y. Gong, H. Wang, J. Jin, *Small* 2025, **21**, e06854.
33 H. Ren, Q. Zhou, Y. Li, L. Zheng, Q. Ni, Q. Li, J. Qian, S. Li, Y. Zhao, F. Wu, C. Wu, Y. Bai, *Energy Storage Mater.* 2025, **76**, 104095.
34 H. Wang, J. Gao, Y. Mei, L. Ni, Y. He, N. Hong, J. Huang, W. Deng, G. Zou, H. Hou, T. Liu, C. Liang, X. Ji, K. Amine, *Angew. Chem. Int. Ed.* 2025, **64**, e202418605.
35 Y. Wang, X. Zhao, J. Jin, Q. Shen, Y. Hu, X. Song, H. Li, X. Qu, L. Jiao, Y. Liu, *J. Am. Chem. Soc.* 2023, **145**, 22708-22719.
36 T. Zhang, M. Ren, Y. Huang, F. Li, W. Hua, S. Indris, F. Li, *Angew. Chem. Int. Ed.* 2024, **63**, e202316949.
37 X. Jia, Q. Peng, Y. Liu, D. Chen, J. Wang, J. Li, Y. Zhu, N. Xu, L. Kong, H. Liu, G. Zhang, Z. Jian, C. Cheng, H. Dong, L. Zhang, Y. Sun, S. Chen, X. Guo, S. Dou, Y. Xiao, *Nat. Commun.* 2025, **16**, 10477.
38 X. Wang, H. Li, Z. Dai, J. Li, Y. Song, B. Han, X. Wang, J. Chen, C. Dong, Z. Mao, L. Zhang, *Energy Storage Mater.* 2025, **79**, 104345.
39 D. Yang, C. Liu, X. Gao, Z. Zhao, Q. Gu, Y. Long, Q. Lai, H. Chen, Z. Liu, W. Luo, *Angew. Chem. Int. Ed.* 2025, **64**, e202500939.
40 G. Liu, W. Xu, J. Wu, Y. Li, L. Chen, S. Li, Q. Ren, J. Wang, *Journal of Energy Chemistry* 2023, **83**, 53-61.
41 Q. Huang, D. Cheng, B. Wu, Z. Liu, K. Zhang, Y. Zou, L. Li, Y. Chen, *Adv. Funct. Mater.* 2025, DOI: 10.1002/adfm.202518419.
42 L. He, F. Song, Y. Cao, Q. Chen, *Energy Storage Mater.* 2025, **80**, 104370.
43 Y. Dong, Z. Zhou, Y. Ma, H. Zhang, F. Meng, Y. Wu, Y. Ma, *ACS Energy Lett.* 2024, **9**, 5096-5119.
44 K. Zhang, J. Zou, Z. Xu, G. Liu, L. He, Q. Yu, F. Wang, Y. Xia, *J. Am. Chem. Soc.* 2025, **147**, 48147-48157.
45 W. Lai, F. Luo, L. Zeng, Z. Lai, K. Jia, F. Xiao, L. Chen, Y. Lu, Q. Qian, Q. Chen, K. Zhang, Z. Yan, J. Chen, *Adv. Funct. Mater.* 2025, DOI: 10.1002/adfm.202517602.
46 J. Huang, Z. Xue, S. Lee, H. Chen, X. Ji, K. Du, *J. Am. Chem. Soc.* 2025, **147**, 22444-22452.
47 X. Zhang, Y. Qiao, S. Guo, K. Jiang, S. Xu, H. Xu, P. Wang, P. He, H. Zhou, *Adv. Mater.* 2019, **31**, 1807770.
48 Y. Huang, F. Zhang, X. Xu, Y. Wang, P. Sun, K. Jing, F. Wu, Z. An, X. Han, Y. Cao, Y. Liu, X. Liao, Y. Li, Z. Xu, Z. Lu, *Energy Storage Mater.* 2025, **83**, 104641.
49 S. Gao, Z. Zhu, H. Fang, K. Feng, J. Zhong, M. Hou, Y. Guo, F. Li, W. Zhang, Z. Ma, F. Li, *Adv. Mater.* 2024, **36**, 2311523.
50 X. Zhang, F. Xie, J. Han, X. Wang, T. Liu, J. Yu, L. Zhang, *Small* 2025, **21**, 2502292.
51 X. Liang, X. Song, H. H. Sun, H. Kim, M. Kim, Y. Sun, *Nat. Commun.* 2025, **16**, 3505.
52 H. Bi, X. Sun, B. Zhao, R. Li, Y. Zhang, X. Wang, M. Zhang, D. Luo, Z. Chen, *Adv. Energy Mater.* 2025, **15**, 2501229.
53 L. Zhang, Y. Hong, J. Xu, S. Lin, Z. Lin, L. Zheng, H. Yao, Z. Hong, *Energy Storage Mater.* 2025, **82**, 104556.
54 F. Ding, P. Ji, Z. Han, X. Hou, Y. Yang, Z. Hu, Y. Niu, Y. Liu, J. Zhang, X. Rong, Y. Lu, H. Mao, D. Su, L. Chen, Y. Hu, *Nat. Energy* 2024, **9**, 1529-1539.
55 T. Yuan, P. Li, Y. Sun, H. Che, Q. Zheng, Y. Zhang, S. Huang, J. Qiu, Y. Pang, J. Yang, Z. Ma, S. Zheng, *Adv. Funct. Mater.* 2025, **35**, 2414627.
56 C. Cai, X. Li, J. Li, R. Yu, P. Hu, T. Zhu, T. Li, S. Lee, N. Xu, H. Fan, J. Wu, L. Zhou, L. Mai, K. Amine, *Nat. Commun.* 2025, **16**, 100.
57 X. Yuan, Y. Guo, L. Gan, X. Yang, W. He, X. Zhang, Y. Yin, S. Xin, H. Yao, Z. Huang, Y. Guo, *Adv. Funct. Mater.* 2022, **32**, 2111466.
58 L. Yu, Y. Chang, M. Liu, Y. Feng, D. Si, X. Zhu, X. Wang, P. Wang, S. Xu, *ACS Appl. Mater. Interfaces* 2023, **15**, 23236-23245.
59 Z. Song, S. Kansara, S. Cheng, M. Yang, F. Li, C. Qi, S. Li, J. Hwang, Y. Bai, *ACS Energy Lett.* 2025, **10**, 5199-5208.
60 H. Wang, H. Chen, Y. Mei, J. Gao, L. Ni, N. Hong, B. Zhang, F. Zhu, J. Huang, K. Wang, W. Deng, D. Silvester, C. Banks, S. Yasar, B. Song, G. Zou, H. Hou, X. Ji, *ACS Nano* 2024, **18**, 13150-13163.
61 L. Yao, P. Zou, C. Wang, J. Jiang, L. Ma, S. Tan, K. Beyer, F. Xu, E. Hu, H. Xin, *Adv. Energy Mater.* 2022, **12**, 2201989.
62 J. Wang, F. Xu, X. Fan, C. Zheng, Y. Zhao, L. Zuo, X. Yun, D. Lu, P. Xiao, Y. Chen, *Chem. Eng. J.* 2024, **500**, 157032.
63 Y. Wu, H. Hu, J. Li, H. Dong, Y. Zhu, S. Chen, N. Wang, J. Wang, Y. Xiao, *Chem. Sci.* 2025, **16**, 3928-3937.
64 J. Kuang, Z. Liu, L. Fu, Y. Shi, M. Zhang, Y. Wang, N. Ding, D. Sun, Y. Tang, H. Wang, *Angew. Chem. Int. Ed.* 2025, **64**, e202500715.
65 W. Xu, C. Cheng, L. Wang, T. Chen, Z. Zhou, T. Yan, S. Shen, P. Zeng, L. Zhang, *Adv. Energy Mater.* 2026, **16**, e04557.
66 H. Hu, M. Yang, D. Chen, N. Xu, J. Li, Y. Zhu, Y. Wu, H. Dong, J. Wang, C. Yao, Y. Yan, S. Chen, N. Wang, W. K. Pang, Y. Sun, J. Wang, Y. Xiao, *Angew. Chem. Int. Ed.* 2026, **65**, e19108.
67 T. Yuan, S. Li, Y. Sun, J. Wang, A. Chen, Q. Zheng, Y. Zhang, L. Chen, G. Nam, H. Che, J. Yang, S. Zheng, Z. Ma, M. Liu, *ACS Nano* 2022, **16**, 18058-18070.
68 S. Zhao, F. Ning, X. Yu, B. Guo, R. Teófilo, J. Huang, Q. Shi, S. Wu, W. Feng, Y. Zhao, *Angew. Chem. Int. Ed.* 2025, **64**, e202416290.
69 S. Gao, Y. Huang, J. Geng, W. Hu, K. Feng, J. Zhong, C. Yu, F. Li, *ACS Energy Lett.* 2025, **10**, 4140-4147.
70 T. Zhang, Z. Song, Y. Li, Y. Huang, J. Su, W. Hua, F. Li, *Angew. Chem. Int. Ed.* 2025, **64**, e202509816.
71 H. Wang, T. Liu, H. Chen, Y. Mei, J. Gao, L. Ni, N. Hong, J. Huang, X. Hu, W. Deng, G. Zou, H. Hou, D. Silvester, C. Banks, X. Ji, K. Amine, *Nat. Commun.* 2025, **16**, 4409.
72 X. Song, R. Liu, J. Jin, X. Zhao, Y. Wang, Q. Shen, Z. Sun, X. Qu, L. Jiao, Y. Liu, *Energy Storage Mater.* 2024, **69**, 103377.
73 A. Zeng, N. Li, H. Zhang, S. Qiu, Z. Xu, Y. Zhang, W. Yin, E. Zhao, X. Xiao, *Angew. Chem. Int. Ed.* 2025, **64**, e202514220.
74 Y. Yang, Z. Wang, C. Du, B. Wang, X. Li, S. Wu, X. Li, X. Zhang, X. Wang, Y. Niu, F. Ding, X. Rong, Y. Lu, N. Zhang, J. Xu, R. Xiao, Q. Zhang, X. Wang, W. Yin, J. Zhao, L. Chen, J. Huang, Y. Hu, *Science* 2024, **385**, 744-752.

View Article Online
DOI: 10.1039/D6SC01783E

The data supporting the findings of this study are available within the article or its supplementary materials.